10-17-2013

Ionospheric Signatures of Acoustic Waves Generated by Transient Tropospheric Forcing

M. D. Zettergren
Embry-Riddle Aeronautical University, zettergm@erau.edu

J. B. Snively
Embry-Riddle Aeronautical University, snivelyj@erau.edu

Ionospheric signatures of acoustic waves generated by transient tropospheric forcing

M. D. Zettergren[1] and J. B. Snively[1]

Received 13 September 2013; accepted 1 October 2013; published 17 October 2013.

[1] Acoustic waves generated by tropospheric sources may attain significant amplitudes in the thermosphere and overlying ionosphere. Although they are weak precursors to gravity waves in the mesosphere below, acoustic waves may achieve temperature and vertical wind perturbations on the order of approximately tens of Kelvin and m/s throughout the *E* and *F* regions. Their perturbations to total electron content are predicted to be detectable by ground-based radar and GPS receivers; they also drive field-aligned currents that may be detectable in situ via magnetometers. Although transient and short lived, ionospheric signatures of acoustic waves may provide new and quantitative insight into the forcing of the upper atmosphere from below.
Citation: Zettergren, M. D., and J. B. Snively (2013), Ionospheric signatures of acoustic waves generated by transient tropospheric forcing, *Geophys. Res. Lett.*, *40*, 5345–5349, doi:10.1002/2013GL058018.

1. Introduction

[2] The existence of acoustic waves (periods ∼1–5 min) and gravity waves (periods >4 min) in the ionosphere above active tropospheric convection has been appreciated for more than 40 years [e.g., *Georges*, 1973, and references cited therein]. Gravity waves, with periodicities >4 min, have recently been found via novel *D* region VLF sensing methods [*Lay and Shao*, 2011] and *F* region GPS total electron content (TEC) measurements [*Lay et al.*, 2013]. Likewise, gravity waves exhibiting distinct concentric ring structures have been identified in mesospheric/lower thermospheric (MLT) airglow data, with curvature of the gravity wave phase fronts revealing proximity above tropospheric convection [e.g., *Yue et al.*, 2013, and references cited therein].

[3] Numerical 3-D models of tropospheric convection confirm that spatially isolated systems produce gravity waves [*Piani et al.*, 2000]. Numerical 2-D cylindrically axisymmetric models also reveal generation of gravity waves [*Walterscheid et al.*, 2001] and infrasonic-acoustic waves [*Walterscheid et al.*, 2003] above simple thermal forcing, with periods of tens of seconds to several minutes that propagate into the thermosphere. Acoustic and gravity waves have also been investigated in compressible ray-tracing studies of propagation from simulated convective plumes [e.g., *Vadas*, 2013]. Modeling studies of acoustic and gravity waves generated simultaneously by transient updrafts suggest that acoustic waves may at times be detectable via airglow imaging as precursors to gravity waves exhibiting cylindrical symmetry [*Snively*, 2013].

[4] Acoustic waves (henceforth AWs) are also generated by transient earthquake and oceanic forcing; their signatures, along with those of gravity waves, were clearly detected in ionospheric electron density following the Tohoku earthquake and tsunami [e.g., *Galvan et al.*, 2011; *Tsugawa et al.*, 2011; *Matsumura et al.*, 2011, and references cited therein]. In situ satellite measurements revealed AWs in the *F* region, with periods ∼1 min, perturbing neutral density by up to ∼11% with vertical velocities ∼130 m/s [*Garcia et al.*, 2013].

[5] This present study aims to provide guidance on the identification of ionospheric AWs generated by tropospheric forcing. We investigate, using coupled atmospheric and ionospheric numerical models, the observable features of AWs generated by idealized transient tropospheric updrafts, which arrive in the mesosphere and thermosphere as precursors to slower gravity waves [e.g., *Snively*, 2013]. We quantify their expected perturbations to electron density and ionospheric vertical total electron content (vTEC), the effects of mid- and low-latitude field geometries, and generation of field-aligned currents.

2. Numerical Model Formulation

2.1. Compressible Neutral Dynamics Model

[6] Numerical simulations are performed with the nonlinear, compressible, atmospheric model of *Snively* [2013], based on the "f-wave" finite volume method (FVM) of *Bale et al.* [2002] and *LeVeque* [2002] and implemented within the Clawpack software package [http://www.clawpack.org]. It solves the Euler equations of conservation of mass, momentum, and energy in a cylindrically axisymmetric domain, including viscosity and thermal conduction, and supports propagation of steep AWs without formation of artifacts. The domain extends from 0 to +450 km in radius r and 0 to +450 km in altitude z, with equal $dr = dz = 500$ m cell dimensions. Boundaries at $r = 450$ km, and $z = 450$ km are "open" and the ground at $z = 0$ km is a reflecting surface.

2.2. Multifluid Ionospheric Model

[7] The multifluid ionospheric model used in this study is an extension of that described by *Zettergren and Semeter* [2012]. It solves the time-dependent, nonlinear equations of conservation of mass, momentum, and energy for seven ion species: $O^+, NO^+, N_2^+, O_2^+, N^+, H^+$, and e^-. It includes all chemical and collisional interactions with the neutral

[1]Department of Physical Sciences, Embry-Riddle Aeronautical University, Daytona Beach, Florida, USA.

Corresponding author: M. D. Zettergren and J. B. Snively, Department of Physical Sciences, Embry-Riddle Aeronautical University, 600 S. Clyde Morris Blvd., Daytona Beach, FL 32114, USA. (zettergm@erau.edu; snivelyj@erau.edu)

0094-8276/2013/10.1002/2013GL058018

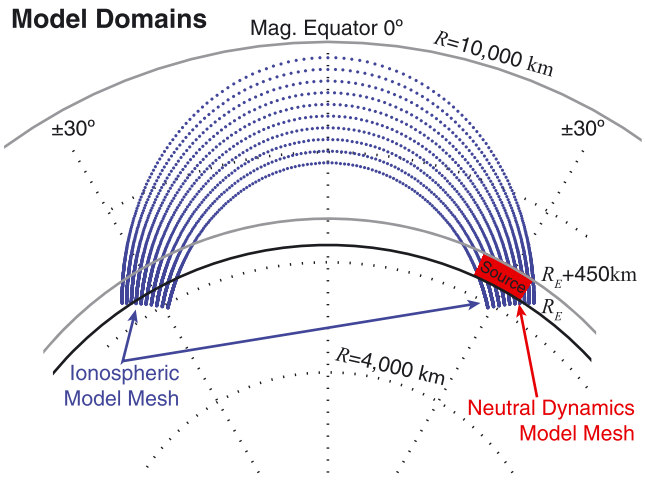

Figure 1. Dipole magnetic field coordinate system of the ionospheric model, shown with superposed radial "slice" through a rotation of the cylindrically axisymmetric neutral dynamics model. The source is placed either in the winter (Northern) hemisphere or summer (Southern) hemisphere.

atmosphere and the effects of thermal conduction in each population. For the present study, the model has been adapted for low latitudes and now includes a dipole magnetic field coordinate system, conservation equations for the proton species, and a photoionization module. Like the neutral dynamics model, it utilizes a flux-limited FVM approach and is thus able to resolve steep nonlinear wave features. The fluid portion of the ionospheric model is supplemented by an electrostatic equation that accounts for the effects of dynamos from neutral wind fields.

[8] The neutral dynamics model drives wind velocity perturbations within the ionospheric model. Figure 1 depicts the embedded dynamics model within the ionospheric model domain, which bisects an axisymmetric rotation of the AW-perturbed fields. Thus, the projection of the neutral model shown in this figure corresponds to a square cross-sectional cut through the cylindrical domain in the plane containing the source of the AWs. The 2-D ionosphere is, therefore, driven only in the meridional direction.

[9] Boundary conditions for the electrostatic equation are zero field-aligned current at ends of each magnetic field line (the "top" and "bottom") and zero potential on the sides corresponding to minimum and maximum L shell. Velocities are set to zero at the ends of the field lines and the sides are free flow boundaries. Ion temperatures are assumed equal to neutral temperature at the ends of the field lines.

2.3. Ambient Atmosphere and Ionosphere

[10] NRLMSISE00 temperature and neutral density profiles are specified for 18°N latitude, 67°W (Northern Hemisphere) and 38°S latitude, 67°W (Southern Hemisphere) on 1 January 2010 at 10:30 UT [*Hedin*, 1991; *Picone et al.*, 2002]. The waves studied here are not sensitive to specific conditions, and we assume that intervening winds would not strongly influence their upward propagation due to high acoustic phase velocities.

[11] The ambient ionosphere is calculated self-consistently from solar conditions, and NRLMSISE00 neutral atmospheric densities and temperature in the regions spanned by the model (note that the large domain in Figure 1 requires that neutral atmospheric parameters vary with respect to geographic location). For the cases examined, summer/winter asymmetries in plasma density and conductivity, due to varying solar zenith angles (~74° in the Southern Hemisphere and ~96° in the Northern Hemisphere) and background neutral atmospheric conditions, play important and apparent roles in the response of the ionosphere.

2.4. Wave Source Characteristics

[12] The wave source corresponds with a single updraft and subsequent atmospheric response and is applied via forcing near the tropopause. It appears in the vertical momentum equation as a "body force" term [e.g., *Vadas*, 2013] proportional to density, $F_z = \rho A(r,z,t)$. The source is defined by a simple vertical acceleration of Gaussian form $A = A_o \exp\left[-(r-r_o)^2/2\sigma_r^2 - (z-z_o)^2/2\sigma_z^2 - (t-t_o)^2/2\sigma_t^2\right]$, where A_o is peak acceleration, σ_r and σ_z are radial and vertical half widths (standard deviations), respectively, and σ_t is the temporal half width. The source is positioned at $r_o = 0$ km and $z_o = 12$ km, where t_o corresponds to its maximum in time.

[13] For real convective systems, a broad spectrum of interacting waves are excited, which propagate in a spatiotemporally varying atmosphere. Identical to that of "Case I" presented by *Snively* [2013], our source excites only a fraction of a realistic spectrum to illustrate the observable signatures of AWs. It is specified by $\sigma_r = 5$ km, $\sigma_z = 3$ km, and $\sigma_t = 60$ sec, where peak forcing occurs at $t_o = 300$ sec, with amplitude $A_o = 0.125$ N·kg^{-1}. The source is slightly shorter in time scale than the fast "plume" sources investigated by *Vadas* [2013], with a full width at half maximum of 2.355 min. It excites a spectrum of gravity waves with periods >5 min and AWs with periods ~3.5 min.

3. Results

[14] Two simulations are presented: First, with the wave source in the summer Southern hemisphere (SSH) and second, with the source in the winter Northern hemisphere (NWH).

[15] Figure 2 depicts resulting velocities and currents in the ionospheric model coordinate system, for the case of the source placed in the SSH. Figure 2a depicts the field-perpendicular neutral gas velocity (field-parallel not shown), taken at a time of 572 s. The AW velocity perturbations are asymmetric with respect to the geomagnetic field, with stronger perpendicular winds poleward of the disturbance (Figure 2a) and stronger parallel winds equatorward (not shown). Figure 2b confirms the static state of the conjugate NWH, which is here unperturbed. Figure 2c reveals field-aligned currents (FACs) driven by the AW perturbation cross section in the SSH and, in Figure 2d, the corresponding NWH conjugate response at reduced amplitude. The associated currents are on the order of tenths and hundredths of μAm^{-2}, respectively. The somewhat stronger FAC response poleward of the wave source in the SSH is due to the stronger perpendicular winds. This feature has an "image" in the NWH from interhemispheric coupling of the currents. Pederson currents in the source hemisphere (not shown) have values of ~±0.01 μAm^{-2} and in the conjugate hemisphere are ~±0.001 μAm^{-2}. For this instance, the conjugate hemisphere currents close primarily through the F region as

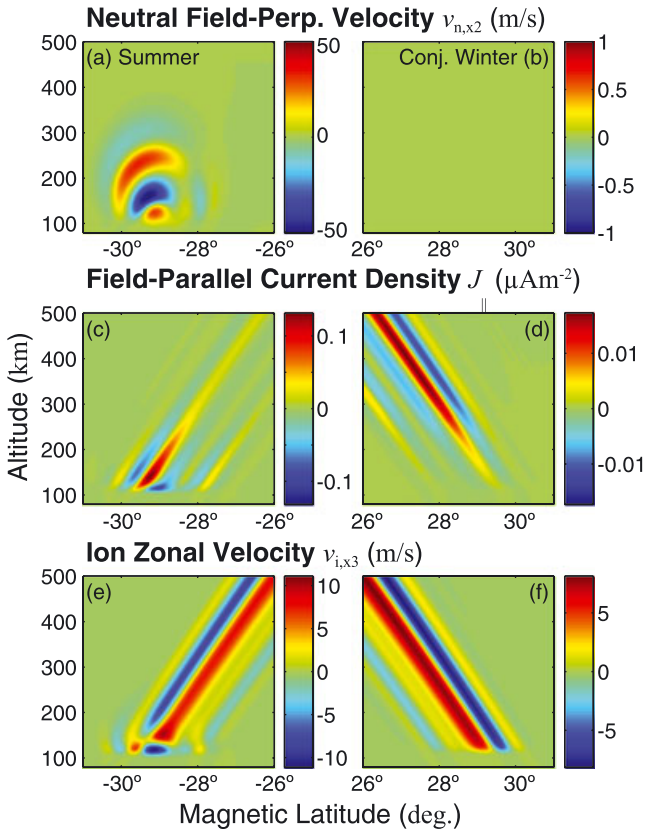

Figure 2. Depiction of model neutral gas velocity perpendicular to geomagnetic field lines in (a) summer (source) and (b) winter (conjugate) hemispheres. Field-aligned current densities are evident in both (c) summer and (d) winter hemispheres; nonzero ion zonal velocities in both (e) summer and (f) winter hemispheres suggest the importance of three-dimensionality.

implied by Figure 2d. Analysis of Joule dissipation rates ($\mathbf{J} \cdot \mathbf{E}$) reveals that the generator region at this time is the source hemisphere *E* region, while both the source and conjugate *F* regions show net dissipation of electromagnetic energy (as well as the conjugate *E* region).

[16] Figures 2e and 2f depict ion zonal velocities for the case of a source in the SSH, calculated from the Hall drift induced by the meridional dynamo electric field. Note the interhemispheric mapping of the electric fields ($\sim\pm0.25$ mV/m in the *F* regions) and $\mathbf{E} \times \mathbf{B}$ drifts. These would also include a component from the zonal electric field in a fully 3-D model but are included here merely for illustration. These drifts, while not insignificant, are a factor of 4–8 weaker than field-perpendicular and field-parallel velocities and are of similar scale size. Thus, it is expected that the 2-D models capture the dominant response of the ionosphere in the meridional plane. They also suggest the possible importance of a structured 3-D plasma response in both the directly driven and conjugate hemispheres, which will be investigated in future studies.

[17] Detailed analyses for the case of a NWH source (not shown) show much smaller perturbed values for all electrodynamic parameters. The smaller photoionization source results in lower conductance and substantially reduced dynamo action by the AW. Values for FACs in the NWH source hemisphere are ±0.01 μAm^{-2}, with Pederson currents of ±0.005 μAm^{-2}. Conjugate hemisphere values for FAC are ±0.0075 μAm^{-2}, with Pederson current of ±0.001 μAm^{-2}. Mapped electric fields have values of ±0.02 mV/m, giving $\mathbf{E} \times \mathbf{B}$ drifts of ±0.5 m/s.

[18] Figures 3a–3c depicts the *F* region electron density as it is perturbed by AWs generated by a source in the SSH. Figures 3d–3f depicts the electron density perturbations by AWs generated by an equivalent source in the NWH. For both cases, an equatorward preference is clearly revealed, which results because the field-aligned projection of the neutral wind velocity is largest in this direction. This effectively lifts the plasma along the field line (or pushes it down) through ion-neutral drag forces. The maximum electron density perturbations for both the summer and winter source

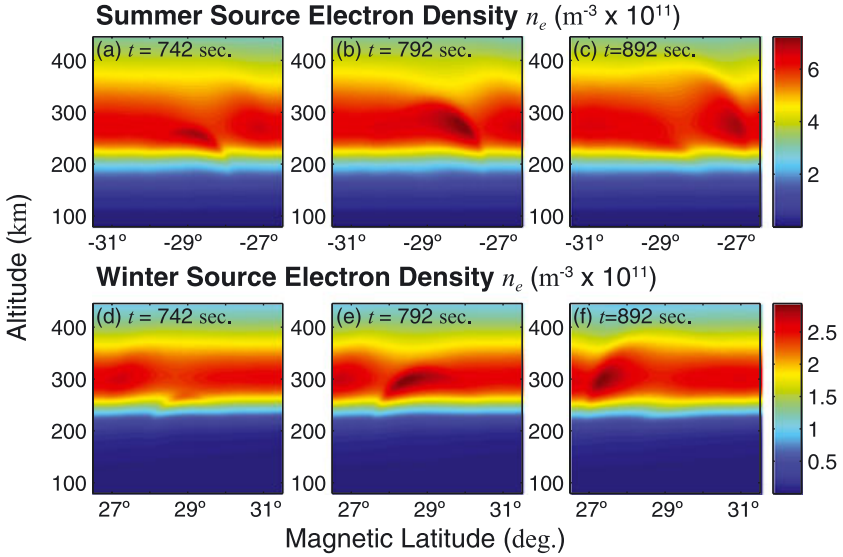

Figure 3. Evolving *F* region electron density perturbations by the acoustic waves for sources positioned in the (a, b, c) summer and (d, e, f) winter hemispheres, revealing preferential perturbations in the equatorward directions.

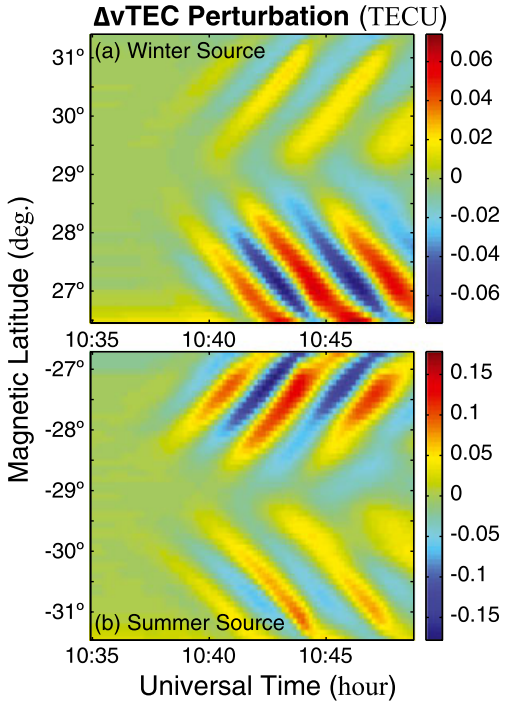

Figure 4. Vertical TEC perturbations (mean subtracted) for latitudes near to the (a) winter and (b) summer hemispheres source locations, revealing stronger perturbations in the post-sunrise SSH ionosphere.

cases are in the range ∼10–25% of background (cf. Figures 3b and 3e) and show very sharp features along the steepened, leading edge of the AW fronts. Absolute differences in electron densities between hemispheres are due to solar zenith angle differences (see section 2.3).

[19] Figure 4 depicts vertical total electron content (vTEC) perturbations near to the source, when it is positioned at either the (Figure 4a) NWH or (Figure 4b) SSH. Notably, in both cases the strongest perturbations to vTEC occur in the equatorward direction, as wave perturbations are enhanced along field lines. This suggests an observable anisotropy in the ionospheric response to the wave, which should not be confused with directionality imposed by the AW radiation and dispersion characteristics. In this case, the SSH perturbations are stronger due to a more intense photoionization source shortly after sunrise. The TEC perturbations for both simulations show an apparent propagation speed consistent with the sound speed in the thermosphere.

4. Discussion and Conclusions

[20] Ionospheric signatures of AWs, generated by a simple tropospheric updraft, have been simulated via a coupled nonlinear compressible atmospheric model and a multifluid ionospheric model. Results demonstrate TEC signatures that are strongest for waves in the magnetic-equatorward meridional direction and imminently observable via GPS. This result appears superficially consistent with interpretations of earthquake-generated TEC perturbations [*Hasbi et al.*, 2009]. The equatorward preference results from the roughly spherical AW phase fronts, which direct a larger field-aligned velocity projection towards the equator. More directive sources, yielding waves with approximately planar phase fronts, may produce TEC responses with a different character [e.g., *Imtiaz and Marchand*, 2012]. Electron density fluctuations in the source hemisphere are ∼10% and large enough to be observable via high time and range resolution incoherent scatter radar experiments [e.g., *Djuth et al.*, 2010]; no significant electron signatures are present in the conjugate hemispheres.

[21] In modeling the FACs, an electrostatic response has been assumed, which is justified on the basis that the dominant AW period is a factor of ∼15 longer than the interhemispheric two-way Alfvén travel time. Moreover, for the SSH source, the reflection coefficient at the conjugate ionosphere appears to be small enough to allow fairly efficient coupling and quick relaxation to a steady state. These conditions are dependent on seasonal and solar conditions and will not always be met, suggesting the need for an electrodynamic treatment especially for longer transits or shorter periods [*Jacobson*, 1986].

[22] Previous studies by *Iyemori et al.* [2005] have suggested that field line resonances may be excited by AWs at shorter periods. The AWs here have periods (∼ 3.5 min) notably longer than the field line resonant period (∼ 15 s). For waves at larger amplitudes, their steepening through the ionosphere may enhance the short-period wave spectrum to approach field line resonance periods. Steepened perturbations of the AW, due to nonlinearity, also enhance the resulting density perturbations (which depend on scale sizes for wind field variations along the geomagnetic field) and wave-driven currents (which depend on scale sizes perpendicular to **B**). Indeed, interhemispheric effects and three-dimensionality of response (from zonal drifts) will be nonlinearly dependent on wave scale and amplitude, in addition to conjugate conductance and seasonal and diurnal variability. These nonlinear interactions and dependencies are well beyond the scope of the present study and will be addressed in future investigations.

[23] Although meteorological sources of AWs remain poorly characterized, the existence of AWs at ionospheric heights has been confirmed previously via their spectral signatures [e.g., *Georges*, 1973]. Readily available TEC data, together with comprehensive theoretical modeling, may provide quantitative insight into the characteristics of tropospheric AW sources and the energetics of AWs in the ionosphere above and MLT below. Assessment of natural sources of AWs may also provide insight into the ambient spectrum generated by various processes to aid in the detection and unambiguous geolocation of natural hazard events [e.g., *Galvan et al.*, 2011; *Tsugawa et al.*, 2011].

[24] **Acknowledgments.** Research by M. D. Zettergren and J. B. Snively was supported by NSF CAREER grants AGS-1255181 and AGS-1151746, respectively, to Embry-Riddle Aeronautical University.

[25] The Editor thanks two anonymous reviewers for their assistance in evaluating this paper.

References

Bale, D. S., R. J. LeVeque, S. Mitran, and J. A. Rossmanith (2002), A wave propagation method for conservation laws and balance laws with spatially-varying flux functions, *SIAM J. Sci. Comput.*, *24*, 955–978.

Djuth, F. T., L. D. Zhang, D. J. Livneh, I. Seker, S. M. Smith, M. P. Sulzer, J. D. Mathews, and R. L. Walterscheid (2010), Arecibo's thermospheric gravity waves and the case for an ocean source, *J. Geophys. Res.*, *115*, A08305, doi:10.1029/2009JA014799.

Galvan, D. A., A. Komjathy, M. P. Hickey, and A. J. Mannucci (2011), The 2009 Samoa and 2010 Chile tsunamis as observed in the

ionosphere using GPS total electron content, *J. Geophys. Res.*, *116*, A06318, doi:10.1029/2010JA016204.

Garcia, R. F., S. Bruinsma, P. Lognonné, E. Doornbos, and F. Cachoux (2013), GOCE: The first seismometer in orbit around the Earth, *Geophys. Res. Lett.*, *40*, 1015–1020, doi:10.1002/grl.50205.

Georges, T. M. (1973), Infrasond from convective storms: Examining the evidence, *Rev. Geophys. Space Phys.*, *11*(3), 571–594.

Hasbi, A. M., M. A. Momani, M. A. Mohd Ali, N. Misran, K. Shiokawa, Y. Otsuka, and K. Yumoto (2009), Ionospheric and geomagnetic disturbances during the 2005 Sumatran earthquakes, *J. Atmos. Sol. Terr. Phys.*, *71*, 1992–2005, doi:10.1016/j.jastp.2009.09.004.

Hedin, A. E. (1991), Extension of the MSIS Thermosphere Model into the middle and lower atmosphere, *J. Geophys. Res.*, *96*(A2), 1159–1172.

Imtiaz, N., and R. Marchand (2012), Modeling of ionospheric magnetic field perturbations induced by earthquakes, *J. Geophys. Res.*, *117*, A04320, doi:10.1029/2011JA017475.

Iyemori, T., et al. (2005), Geomagnetic pulsations caused by the Sumatra earthquake on December 26, 2004, *Geophys. Res. Lett.*, *32*, L20807, doi:10.1029/2005GL024083.

Jacobson, A. R. (1986), A model for conjugate coupling from ionospheric dynamos in the acoustic frequency range, *J. Geophys. Res.*, *91*(A4), 4404–4412.

Lay, E. H., and X.-M. Shao (2011), Multi-station probing of thunderstorm-generated D-layer fluctuations by using time-domain lightning waveforms, *Geophys. Res. Lett.*, *38*, L23806, doi:10.1029/2011GL049790.

Lay, E. H., X.-M. Shao, and C. S. Carrano (2013), Variation in total electron content above large thunderstorms, *Geophys. Res. Lett.*, *40*, 1945–1949, doi:10.1002/grl.50499.

LeVeque, R. J. (2002), *Finite Volume Methods for Hyperbolic Problems*, Cambridge Univ. Press, Cambridge, UK.

Matsumura, M., A. Saito, T. Iyemori, H. Shinagawa, T. Tsugawa, Y. Otsuka, M. Nishioka, and C. H. Chen (2011), Numerical simulations of atmospheric waves excited by the 2011 off the Pacific coast of Tohoku earthquake, *Earth Planets Space*, *63*(7), 885–889, doi:10.5047/eps.2011.07.015.

Piani, C., D. Durran, M. J. Alexander, and J. R. Holton (2000), A numerical study of three-dimensional gravity waves triggered by deep tropical convection and their role in the dynamics of the QBO, *J. Atmos. Sci.*, *57*(22), 3689–3702.

Picone, J. M., A. E. Hedin, D. P. Drob, and A. C. Aikin (2002), NRLMSISE-00 empirical model of the atmosphere: Statistical comparisons and scientific issues, *J. Geophys. Res.*, *107*(A12), 1468, doi:10.1029/2002JA009430.

Snively, J. B. (2013), Mesospheric hydroxyl airglow signatures of acoustic and gravity waves generated by transient tropospheric forcing, *Geophys. Res. Lett.*, *40*, 4533–4537, doi:10.1002/grl.50886.

Tsugawa, T., A. Saito, Y. Otsuka, M. Nishioka, T. Maruyama, H. Kato, T. Nagatsuma, and K. T. Murata (2011), Ionospheric disturbances detected by GPS total electron content observation after the 2011 off the Pacific coast of Tohoku Earthquake, *Earth Planets Space*, *63*, 875–879, doi:10.5047/eps.2011.06.035.

Vadas, S. L. (2013), Compressible *f*-plane solutions to body forces, heatings, and coolings, and application to the primary and secondary gravity waves generated by a deep convective plume, *J. Geophys. Res. Space Physics*, *118*, 1–21, doi:10.1002/jgra.50163.

Walterscheid, R. L., G. Schubert, and D. G. Brinkman (2001), Small-scale gravity waves in the upper mesosphere and lower thermosphere generated by deep tropical convection, *J. Geophys. Res.*, *106*(D23), 31,825–31,832.

Walterscheid, R. L., G. Schubert, and D. G. Brinkman (2003), Acoustic waves in the upper mesosphere and lower thermosphere generated by deep tropical convection, *J. Geophys. Res.*, *108*(A11), 1392, doi:10.1029/2003JA010065.

Yue, J., L. Hoffmann, and M. J. Alexander (2013), Simultaneous observations of convective gravity waves from a ground-based airglow imager and the AIRS satellite experiment, *J. Geophys. Res. Atmos.*, *118*, 3178–3191, doi:10.1002/jgrd.50341.

Zettergren, M. D., and J. Semeter (2012), Ionospheric plasma transport and loss in auroral downward current regions, *J. Geophys. Res.*, *117*, A06306, doi:10.1029/2012JA017637.